



## Østerild: A natural laboratory for atmospheric turbulence

Peña, Alfredo

*Published in:*  
Journal of Renewable and Sustainable Energy

*Link to article, DOI:*  
[10.1063/1.5121486](https://doi.org/10.1063/1.5121486)

*Publication date:*  
2019

*Document Version*  
Publisher's PDF, also known as Version of record

[Link back to DTU Orbit](#)

*Citation (APA):*  
Peña, A. (2019). Østerild: A natural laboratory for atmospheric turbulence. *Journal of Renewable and Sustainable Energy*, 11(6), Article 063302. <https://doi.org/10.1063/1.5121486>

---

### General rights

Copyright and moral rights for the publications made accessible in the public portal are retained by the authors and/or other copyright owners and it is a condition of accessing publications that users recognise and abide by the legal requirements associated with these rights.

- Users may download and print one copy of any publication from the public portal for the purpose of private study or research.
- You may not further distribute the material or use it for any profit-making activity or commercial gain
- You may freely distribute the URL identifying the publication in the public portal

If you believe that this document breaches copyright please contact us providing details, and we will remove access to the work immediately and investigate your claim.

# Østerild: A natural laboratory for atmospheric turbulence

Cite as: J. Renewable Sustainable Energy **11**, 063302 (2019); <https://doi.org/10.1063/1.5121486>  
Submitted: 25 July 2019 . Accepted: 01 November 2019 . Published Online: 19 November 2019

A. Peña 



View Online



Export Citation



CrossMark

## ARTICLES YOU MAY BE INTERESTED IN

[Competitive assessment of Indian wind power industry: A five forces model](#)

Journal of Renewable and Sustainable Energy **11**, 063301 (2019); <https://doi.org/10.1063/1.5116237>

[Producing wind energy at the cost of biodiversity: A stakeholder view on a green-green dilemma](#)

Journal of Renewable and Sustainable Energy **11**, 063303 (2019); <https://doi.org/10.1063/1.5118784>

[Classification of the Reynolds stress anisotropy tensor in very large thermally stratified wind farms using colormap image segmentation](#)

Journal of Renewable and Sustainable Energy **11**, 063305 (2019); <https://doi.org/10.1063/1.5113654>

AIP Conference Proceedings  
**FLASH WINTER SALE!**

**50% OFF** ALL PRINT PROCEEDINGS

ENTER CODE 50DEC19 AT CHECKOUT

AIP  
Publishing

# Østerild: A natural laboratory for atmospheric turbulence

Cite as: J. Renewable Sustainable Energy **11**, 063302 (2019); doi: 10.1063/1.5121486

Submitted: 25 July 2019 · Accepted: 1 November 2019 ·

Published Online: 19 November 2019



View Online



Export Citation



CrossMark

A. Peña 

## AFFILIATIONS

DTU Wind Energy, Technical University of Denmark, Roskilde, Denmark

## ABSTRACT

Understanding atmospheric turbulence is without a doubt one of the most complex subjects in meteorology. However, its behavior can be more easily investigated by analysis of high-quality measurements of the velocity and temperature fluctuations. Here, we show that at the large test station of wind turbines in Østerild, northern Denmark, measurements from a 250-m lightning mast provide unique insights into the behavior of atmospheric turbulence within the range of heights where modern large wind turbines operate. We illustrate that for the predominant westerly winds at the site, the flow can be assumed to be close to homogeneous. This allows the analysis of the behavior with atmospheric stability and height of the wind speed and direction and of different turbulence measures, i.e., velocity variances and covariances, as well as turbulence spectra and their characteristics. It is shown, e.g., that for a wide range of atmospheric stability conditions, turbulence parameters up to 241 m are directly related to mean flow characteristics, which will aid in improving the simulation of turbulence in, i.e., aeroelastic simulations. These measurements can be used for the evaluation of a wide range of models describing the meteorological conditions and the atmospheric flow and its turbulent behavior.

© 2019 Author(s). All article content, except where otherwise noted, is licensed under a Creative Commons Attribution (CC BY) license (<http://creativecommons.org/licenses/by/4.0/>). <https://doi.org/10.1063/1.5121486>

## I. INTRODUCTION

Boundary-layer meteorology and, for our particular interest, wind-power meteorology rely on flow and meteorological models that can describe the behavior of atmospheric turbulence as accurate as possible. However, the complexity of the description of atmospheric turbulence hinders the development of models of different fidelities. The development and improvement of such models thus rely heavily on our understanding of turbulence from measurements.

However, high-quality, long-term, and accurate turbulence measurements extending beyond the first tens of meters from the ground are rarely found. Cup anemometers are robust instruments, but they can only measure the horizontal velocity accurately and, thus, only the variance of the horizontal velocity. Sonic anemometers, nowadays almost as robust as cup anemometers, are able to measure all velocity and temperature fluctuations, but due to their measurement configuration, they are affected by self-induced flow distortion.<sup>1,2</sup> Further, when deployed on masts, both cup and sonic anemometers suffer from structure-induced flow distortion.<sup>3</sup> Alternatives to these forms of *in situ* anemometry, which avoid issues of flow distortion, are remote-sensing techniques. Generally, remote sensors are able to probe the atmosphere in much more detail (in terms of vertical spacing) and cover higher ranges than conventional meteorological masts, but their measurement availability is generally lower, and due to the

characteristics of the probe volumes and scanning configuration, their turbulence estimates are normally biased when compared to those from sonic- and cup-anemometer measurements.<sup>4,5</sup>

Although relatively recently established, the measurements performed at the large test station of wind turbines in Østerild, northern Denmark, have already been used for different purposes. Larsén *et al.*<sup>6</sup> used cup and sonic anemometer measurements to analyze the height dependence of the wind speed power spectrum from the synoptic scale to the spectral gap. Karagali *et al.*<sup>7</sup> examined the imprint of surface heterogeneity on the mean wind flow around Østerild by analyzing measurements from two scanning lidars performing horizontal wide scans at 50 and 200 m. The latter campaign is part of the experiments of the New European Wind Atlas.<sup>8</sup> Kelly<sup>9</sup> used sonic anemometer and lidar measurements performed in Østerild, prior to the construction of the test station, to investigate the relation between the turbulence length scale and the mean vertical wind shear. Hannesdóttir and Kelly<sup>10</sup> characterized ramplike wind-speed fluctuations using the sonic anemometer measurements.

Here, the purpose is to introduce the Østerild measurements to boundary-layer and wind-power meteorologists, in particular, those from the sonic anemometers that cover the first 241 m. This is mainly done by analysis of the behavior with the atmospheric stability and height of wind speed, direction, velocity variances, covariances, and

turbulence spectra. Further, we show how turbulence spectral tensor parameters behave with the height and atmospheric stability and the relation of the turbulence length scale with standard wind-power measurements, which is useful to improve the description of the three-dimensional turbulence structure of a given site.

Section II introduces the Østerild facility and the measurements deployed on the lightning meteorological mast. Data handling (selection, filtering, and flow correction) is described in Sec. III. The general wind conditions at the site are described in Sec. IV including yearly and diurnal distributions of atmospheric stability and the behavior of wind speed distributions with the height. Section V describes the land use characteristics of the area and provides estimates of the roughness length for different wind directions. Turbulence intensity and atmospheric stability conditions are examined in Secs. VIA and VIB. Section VIC focuses on the close-to-homogeneous sector at Østerild: the behavior of the vertical profiles of the mean wind and direction is illustrated together with that of the velocity variances and covariances. For the latter sector, the turbulence spectra and their characteristics with height and atmospheric stability are examined in Sec. VIC3. The last section provides some perspectives for future work and conclusions.

## II. THE ØSTERILD FACILITY

### A. Østerild test station

The Østerild test station is located in northern Jutland, Denmark, on a land portion between the waters from Limfjorden and the North Sea [see Fig. 1(a)]. The station mainly consists of seven turbine stands (two more are being added), each with a mast deployed about 2.5–4 rotor diameters west of the turbine reaching the correspondent hub height (see <https://www.vindenergi.dtu.dk/english/test-centers/oesterild> for details of the turbines). The turbines are aligned in the north-south direction extending almost 6 km. Two lightning masts are deployed north and south of the row of turbines. The terrain is flat, as shown in Fig. 1(b), and heterogeneous, with a mix between crop and agricultural land, urban areas, and forest.

### B. The Østerild lightning masts

The Østerild lightning masts are 250-m tall towers with a triangular lattice structure (see Fig. 2). They are equally equipped with instruments at different levels. Here, we are mostly interested in the measurements from the Risø P2546A cup anemometers at 10, 40, 70, 106, 140, 178, 210, and 244 m above the ground level (agl—all heights are here referred to agl unless otherwise stated), a reference wind vane at 40 m, and Metek USA-1 sonic anemometers at 7, 37, 103, 175, and 241 m. The difference between the south and the north mast is that for the first, sonic and cup anemometers are mounted on booms at 180° from the north and for the second at 0°. There are redundant cup anemometers at 106 and 178 m.

## III. DATA HANDLING

### A. Data selection and filtering

The analysis of the velocity and turbulence profiles is based on the sonic anemometer measurements mainly and is performed on 10-min statistics. Therefore, sonic and cup anemometer measurements were extracted when all sonic anemometers deployed on the south lightning mast were available. We focus our analysis on this mast because (1) it has more availability than the north mast (99% vs 71%), (2) the frequency of south winds is higher than that of the north winds

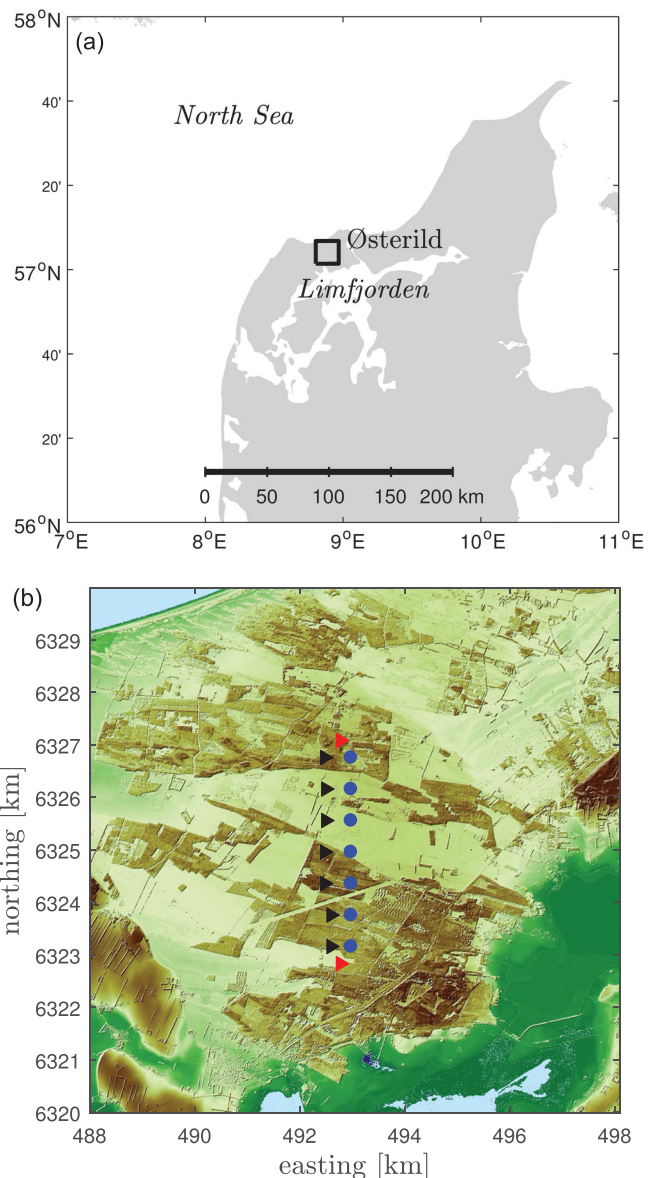


**FIG. 1.** (a) The area of the Østerild test station (black rectangle) in northern Jutland, Denmark. (b) Digital surface model (UTM WGS84) of the area within the black rectangle in frame (a), showing the locations of the turbines (circles), the turbine masts (black triangles), and the lightning masts (red triangles).

(see Sec. IV), and so the wakes from the wind turbines and direct mast shadow influence less often the measurements on the south than those on the north mast, and (3) there is a forest clearance west of the south mast; since the predominant winds at Østerild are westerlies, the flow, to a reasonable extent, can be considered homogeneous at this position. Therefore, we can eventually compare the observations with canonical flow solutions and simulations (see Sec. VIC for details). Our analysis concentrates on observations covering the period starting on April 1, 2015 to March 5, 2019.

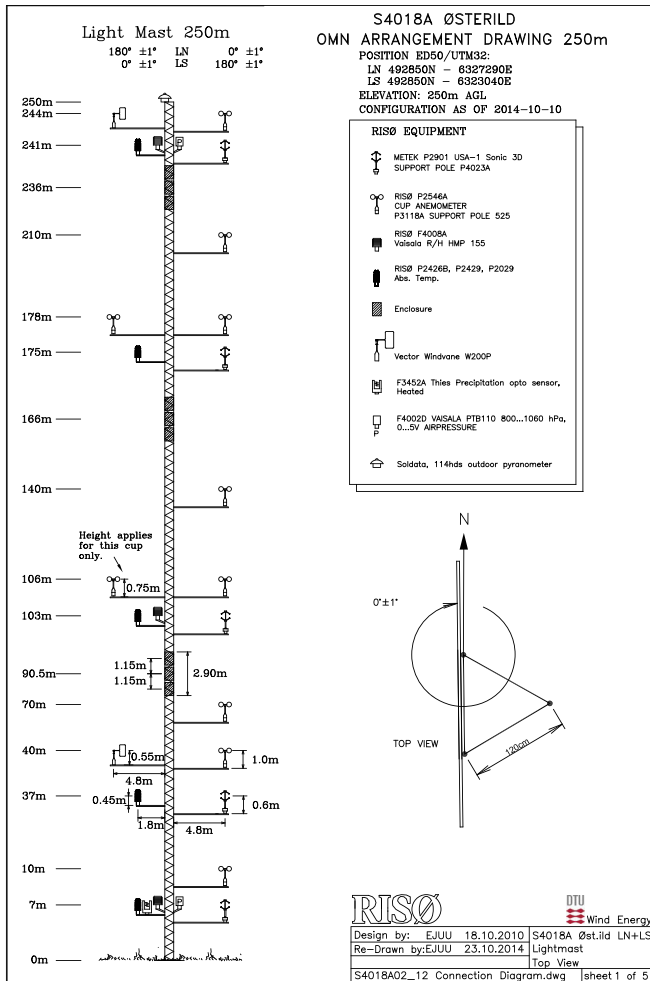


FIG. 2. Illustrative sketch of the lightning masts at Østerild with the instrumentation.

We first filtered data with regard to the minimum observed mean wind speed (hereafter, the term mean refers to the average over a 10-min period); the cup anemometer at 10 m must have recorded wind speeds higher than  $3 \text{ m s}^{-1}$ . 103 936 10-min ( $\approx 24$  months) were left after applying this criterion.

Second, we filtered data with regard to the quality of the sonic anemometer 20 Hz records within a 10-min period; for all records, the sonic anemometer status must have been either 0 or 1, i.e., that new data were acquired by the system without errors. Also, we only allowed complete 10-min time series for the analysis. This means that all sonic-derived statistics were based on 10-min time series containing 12 000 records. A total of 63 427 10-min ( $\approx 15$  months) were left for the analysis.

**B. Correction and usage of sonic anemometer measurements**

For each 10-min period, we removed the 2D correction and applied the 3D correction suggested by METEK GmbH,<sup>11</sup> which was

shown to correct the velocity components in such a way that the ratio of the  $w$ - to the  $u$ -velocity spectrum and that of the  $v$ - to the  $u$ -velocity spectra within the inertial subrange become very close to  $4/3$  as expected from Kolmogorov’s hypothesis.<sup>2</sup> We also applied the corrections suggested by Liu *et al.*<sup>12</sup> for the computation of the sonic heat flux, which we assume to be equal to the virtual potential kinematic heat flux. We applied yaw and pitch rotations to the sonic anemometer 10-min time series, so that the  $u$ -velocity component becomes aligned with the mean wind with the rotation angles determined each 10-min period.

We compute fluctuations of velocities, their variances and covariances, and other turbulent fluxes from the sonic anemometer measurements. The friction velocity is computed as

$$u_* = (\overline{u'w'^2} + \overline{v'w'^2})^{1/4}, \tag{1}$$

where the prime (') denotes fluctuations and the overbar a mean. The Obukhov length is computed as

$$L_O = -\frac{T_s u_*^3}{\kappa g w' T_s'}, \tag{2}$$

where  $T_s$  is the sonic anemometer temperature,  $\kappa$  is the von Kármán constant (we use a value of 0.4), and  $g$  is the earth’s gravitational acceleration. We also compute the three velocity component autospectra and  $uw$ -cospectra. We classified the sonic anemometer observations within atmospheric stability classes by estimating the dimensionless stability parameter  $z/L_O$ , where  $z$  is the height above ground, and using the ranges in Table I.

**C. Mast and wind turbine shading**

Since we concentrate the analysis on the sonic anemometer measurements, we want to avoid the direct mast shadow on the observations and the influence of the wind turbines’ wakes in the stands. Turbine 7, which is the southern in the row, directly shadows the south mast for  $32^\circ$  winds, and thus, assuming a wide wake expansion of  $15^\circ$ , we guarantee a wake-free sector from  $47^\circ$ . Turbine 1 direct “shadow” (if any) is at  $3^\circ$  from the south mast, and so the wake-free sector is within the range of  $47^\circ$ – $348^\circ$ .

Figure 3 shows the ratio of the horizontal wind speed measured by the sonic to the twin cup anemometer at two levels as a function of wind direction (similar results are found for the levels at 103 and 175 m). Three sets of data are shown: a group of 10-min periods within an

TABLE I. Definition of atmospheric stability classes within intervals of dimensionless stability  $z/L_O$ .

Stability class	$z/L_O$
Very unstable (vu)	(−2.0, −0.5)
Unstable (u)	(−0.5, −0.2)
Near unstable (nu)	(−0.2, −0.05)
Neutral (n)	(−0.05, 0.05)
Near stable (ns)	(0.05, 0.2)
Stable (s)	(0.2, 0.5)
Very stable (vs)	(0.5, 2.0)

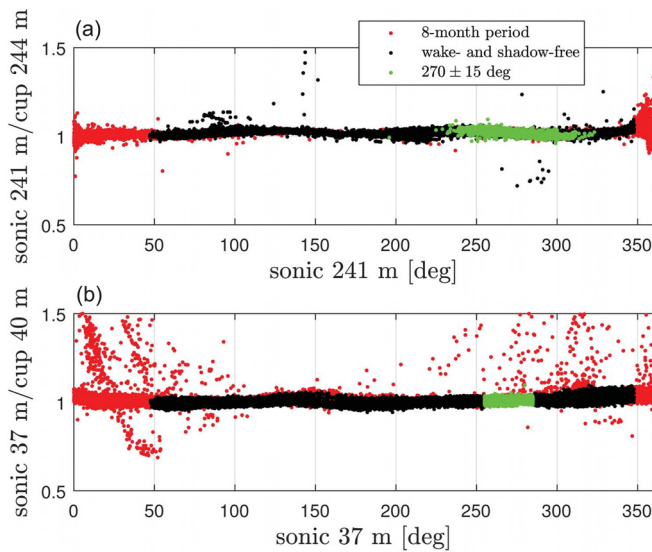


**FIG. 3.** Horizontal wind speed ratio of the sonic to cup anemometer measurements at 241 m (a) and 37 m (b) as a function of the sonic anemometer wind direction. The different colors correspond to 10-min values within either different periods or flow conditions (see the text for details).

eight-month period (November 2015 to June 2016), where the sonic anemometer measurements show a systematic misbehavior, which is clearly illustrated as cup to sonic wind speed ratios are far from one, 10-min periods avoiding the direct influence of turbine wakes and mast shadow, and 10-min periods within the  $270^\circ \pm 15^\circ$  sector with reference to the direction measured by the 37-m sonic anemometer. It is clearly illustrated that most outliers are filtered out by removing data from the eight-month period. For the wake- and shadow-free directions in Fig. 3(a), a few outliers are shown; these correspond to groups of consecutive 10-min periods, and so they might be caused by temporal nonreported data acquisition issues. Data left after filtering the eight-month period and the turbine/mast wake sectors amount for 51 209 10-min ( $\approx 12$  months), and those within the  $270^\circ \pm 15^\circ$  sector are 14 355 10-min ( $\approx 3$  months).

**IV. WIND CONDITIONS**

Figure 4 shows the wind roses from the measurements of two cup anemometers separated 204 m vertically and illustrates the predominance of westerlies at the Østerild site, being the winds from the northern directions, the less frequent. In this section, we analyzed the cup anemometer measurements only, and we do not follow the data filtering criteria described in Sec. III A, since we want to show all possible recorded winds for wind climatology.

Figure 5(a) shows the histogram of wind speed from measurements of a number of cup anemometers together with the distribution of wind speed derived from computing the Weibull scale and shape parameters  $A_w$  and  $k_w$  using a maximum likelihood estimator on the time series. As illustrated, these all-sectors histograms closely follow Weibull distributions. A similar analysis was performed for the sector  $270^\circ \pm 15^\circ$  (not shown), and the Weibull distributions follow even closer the histograms compared to the all-sector analysis.

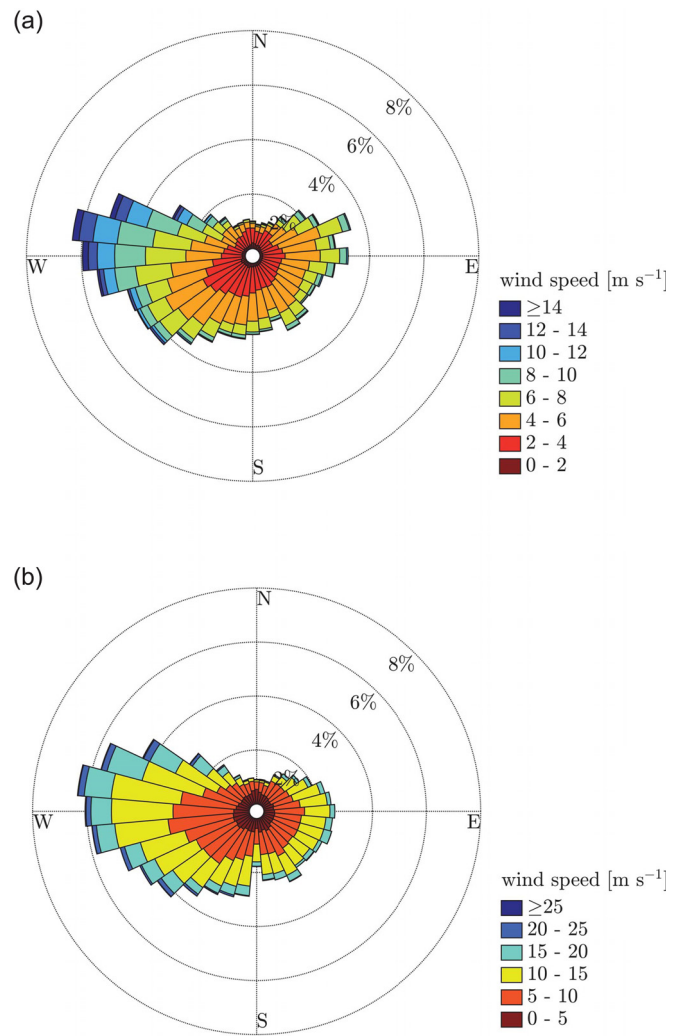


**FIG. 4.** Wind roses observed by the cup anemometers at 40 m (a) and 244 m (b) on the Østerild south lightning mast.

Figures 5(b) and 5(c) show the behavior with the height of the Weibull parameters for both the all and  $270^\circ \pm 15^\circ$  sectors. As expected  $A_w$  increases with the height as it is directly related to the mean wind speed, whereas  $k_w$  increases up to a maximum, the reversal height, and decreases slowly above that level. This behavior combines the effect of the diurnal and the synoptic variation.<sup>13</sup> Interestingly, for the all-sector dataset,  $k_w$  values are slightly lower, and thus, the variability of 10-min mean winds is higher than that for the  $270^\circ \pm 15^\circ$  sector, which is expected due to the heterogeneity of the area.

Figure 6 illustrates the frequency of occurrence of the atmospheric stability classes in Table I based on the observations of the sonic anemometer at 37 m per both month and hour for all wake- and shadow-free sectors. Near-neutral conditions clearly dominate during all months and hours. Stable and very stable conditions are the rarest

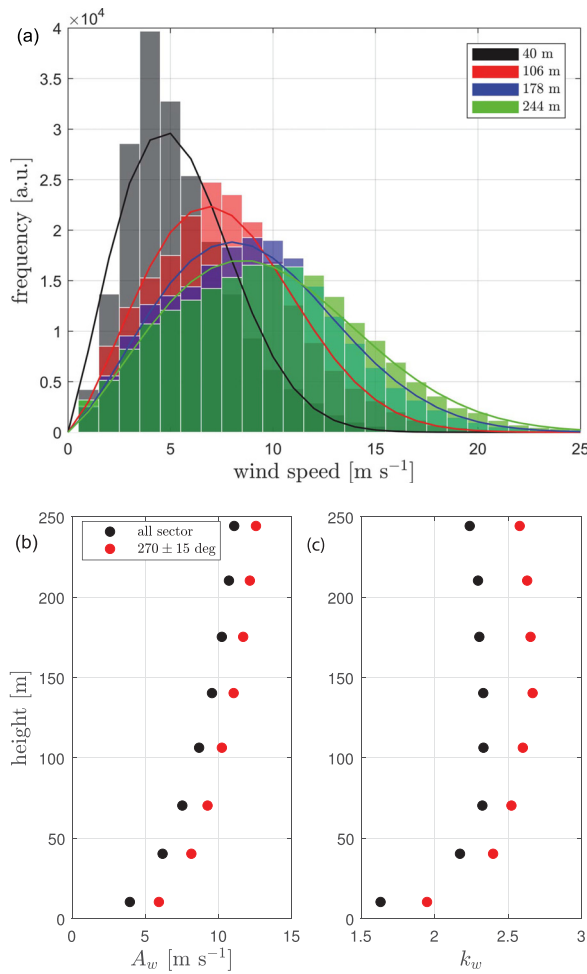


**FIG. 5.** (a) Wind speed histograms from cup anemometer measurements of four selected heights together with the Weibull distribution from a fit to the time series. (b) and (c) Variation with the height of the Weibull parameters  $A_w$  and  $k_w$ , respectively, for both all sectors and the  $270^\circ \pm 15^\circ$  sector.

during all months and disappear nearly completely approaching midday. Unstable and very unstable conditions do rarely appear during the winter months and can be found from 06:00 to 19:00 only, peaking around midday.

**V. ROUGHNESS AND LAND-USE CHARACTERISTICS**

The roughness length can be estimated using different methodologies (e.g., from surface characterization or by analyzing wind measurements). One can derive it also in several ways from observations. Figure 7(a) shows for 30° wind sectors the roughness rose derived using the 7-m sonic anemometer observations and that using the 37-m sonic anemometer observations within neutral atmospheric conditions assuming that the logarithmic wind profile can be applied locally, i.e.,

$$z_0 = \frac{z}{\exp(\kappa U/u_*)}, \tag{3}$$

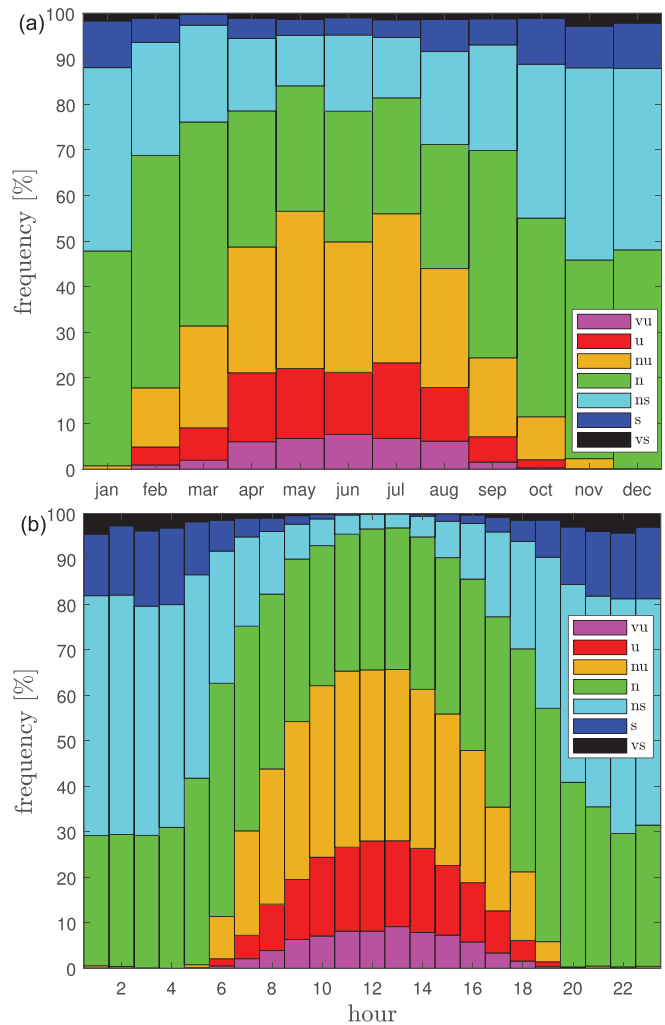


**FIG. 6.** Frequency of occurrence of stability classes based on the 37-m sonic anemometer per month (a) and per hour (b) for wake- and shadow-free sectors.

where  $\kappa$  is the von Kármán constant ( $= 0.4$ ) and  $U = (u^2 + v^2)^{1/2}$  is the magnitude of the mean horizontal wind. For each sector, the value shown in Fig. 7(a) is  $\exp \langle \ln z_0 \rangle$ , which represents an ensemble-average roughness length.

The results for each of the sonic-anemometer observations show different patterns, except that in both cases, the  $270^\circ \pm 15^\circ$  sector shows the lowest values. By using the measurements from the 7-m level, lower  $z_0$ -values are generally found, except for the 120° and 150° sectors. The trees around the south lightning mast are 15–20-m tall, and so the roughness estimation for all but  $270^\circ \pm 15^\circ$  is biased by the displacement height, which cannot be accurately estimated due to the surface heterogeneity.

Figure 7(b) shows the distributions of  $z_0$  computed from Eq. (3) for the  $270^\circ \pm 15^\circ$  sector under neutral stability conditions. The values estimated from the 37-m level are more scattered than those at 7 m, as expected, because more nonlocal effects (e.g., from the surrounding forest and villages) affect the observations. They also show a higher

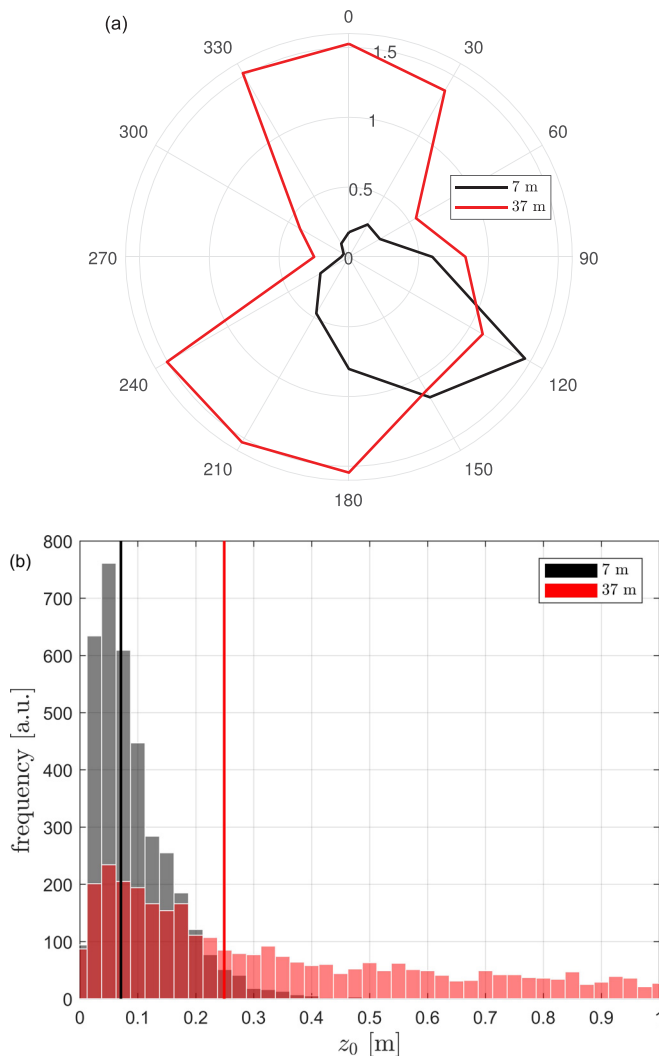


**FIG. 7.** (a) Sector-wise roughness length estimation ( $\exp \langle \ln z_0 \rangle$ ) based on the 7- and on the 37-m sonic anemometer measurements under neutral stability conditions (see the text for details). (b) Distribution of the roughness length estimations in (a) within the  $270^\circ$  sector only. The solid lines correspond to  $\exp \langle \ln z_0 \rangle$  from measurements of either sonic anemometer.

ensemble-average value than those of the 7-m level, illustrating the influence of the high roughness elements on the 37-m level.

Meteorological models, however, rely on land use datasets, and it is up to the model and the “user experience” to assign roughness-length values to given land-use classes. Floors *et al.*<sup>14</sup> discussed a technique, which objectively produces roughness-length maps from tree-height maps that are created using airborne laser scans. The technique basically estimates the elevations of the point cloud within a spatial grid cell of typically  $20 \text{ m} \times 20 \text{ m}$ . The tree height is estimated as the maximum of the difference between the elevation of all points within the grid cell and the median of those points. The roughness map around Østerild in Fig. 8 assumes that the roughness length is 10% the estimated tree height.<sup>15</sup>

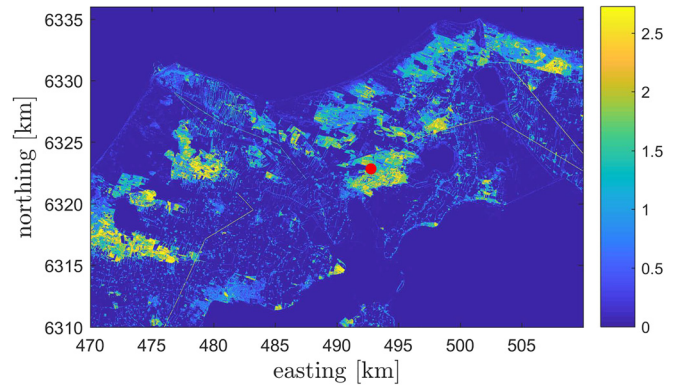


**FIG. 8.** Roughness map of the area around Østerild in northern Denmark (UTM WGS84) derived from airborne laser scans. The location of the south lightning mast is indicated in a red circle. The colorbar indicates the roughness length in meters.

## VI. TURBULENCE CONDITIONS

### A. Turbulence intensity

Figure 9 shows the behavior of the turbulence intensity ( $TI = \sigma_u/U$ , where  $\sigma_u$  is the standard deviation of the  $u$ -velocity component) with wind speed for the different heights and for both the wake- and shadow-free and the  $270^\circ \pm 15^\circ$  sectors. The range of TIs is large ( $\approx 0.05$ – $0.3$ ), which shows the variety of turbulence conditions of the site. For both cases, the TI behavior with wind speed is very similar for the two highest levels and the main differences appear at the lowest three levels. For the latter height ranges, the TI is higher for the broader than for the narrow sector as the forest nearby strongly influences these heights.

Further, for both cases, TI behaves with wind speed as expected; it decreases with increasing wind and decreases with the height. For the three highest levels, the TI tends to stabilize (or even increase) for winds  $\geq 12 \text{ m s}^{-1}$ , which is a behavior typical of near-neutral conditions.<sup>16</sup>

### B. Atmospheric stability

Figure 10 illustrates frequency distributions of the dimensionless stability for both the wake- and the shadow-free and the  $270^\circ \pm 15^\circ$  sectors for the different heights. Although for the narrower sector, the frequencies are more evenly distributed than for the broader sector, both show the same pattern with the height; at 7 m, most conditions are close to neutral ( $z/L_0 \approx 0$ ) and the distributions systematically spread, covering further stable and unstable conditions, the higher the level of the sonic anemometer. For the narrow sector, the ranges of dimensionless stabilities in Table I are also shown.

Figure 11 shows, based on either the 37- or the 241-m sonic anemometer measurements, the occurrence of atmospheric stability classes per wind speed bin for the wake- and shadow-free sectors. Based on the 37-m measurements, the stability conditions are predominantly near-neutral for all wind speed ranges with the very unstable and very stable conditions within the lowest wind speed ranges. Based on the 241-m measurements, however, neutral conditions are generally less predominant within the whole wind speed range, although always present. Unstable and very unstable conditions are predominant within the low wind speed range, and stable and very stable conditions prevail within the high wind speed range.

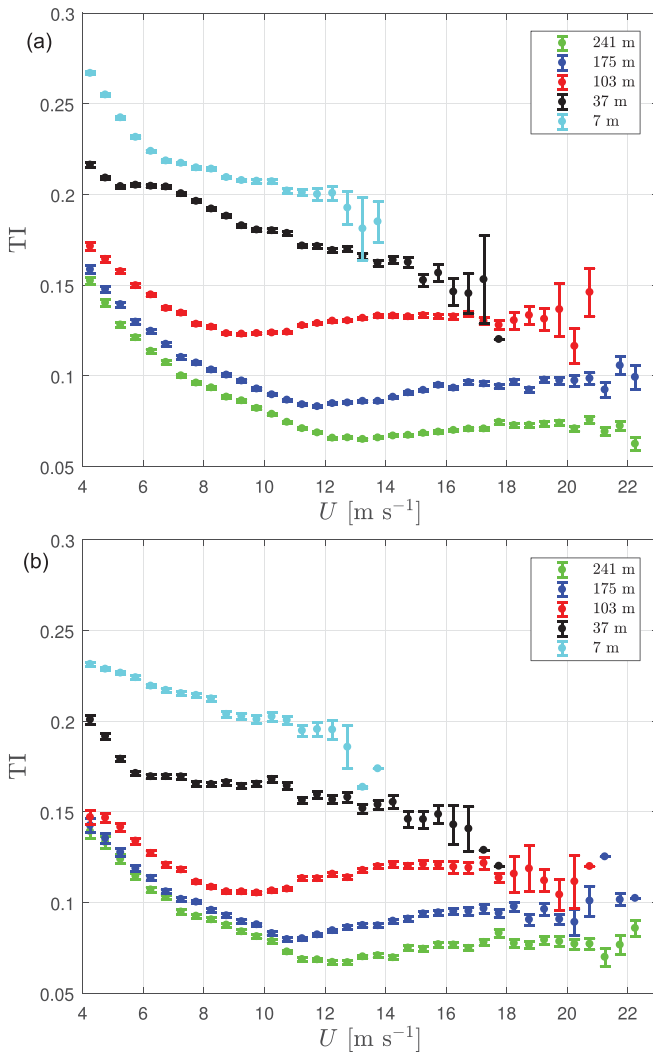


FIG. 9. Turbulence intensity behavior with wind speed for different heights for the wake- and shadow-free (a) and 270° ± 15° (b) sectors. The error bars show ±1 standard error.

### C. Close-to-homogeneous conditions

#### 1. Vertical wind shear

As explained earlier, due to the surface characteristics within the 270° ± 15° sector, we might have the possibility to study canonical flows at Østerild. To understand how homogeneous the atmospheric flow is within this range of directions, we can start by studying the behavior of the surface-layer dimensionless wind shear,

$$\phi_m = \frac{\kappa z dU}{u_* dz}, \quad (4)$$

with dimensionless stability  $z/L_O$ . The dimensionless wind shear should follow surface-layer similarity<sup>17</sup> under homogeneous flow conditions, i.e., it should not deviate largely from the empirical expressions relating both dimensionless parameters.<sup>18</sup> Here,  $dU/dz$  was computed

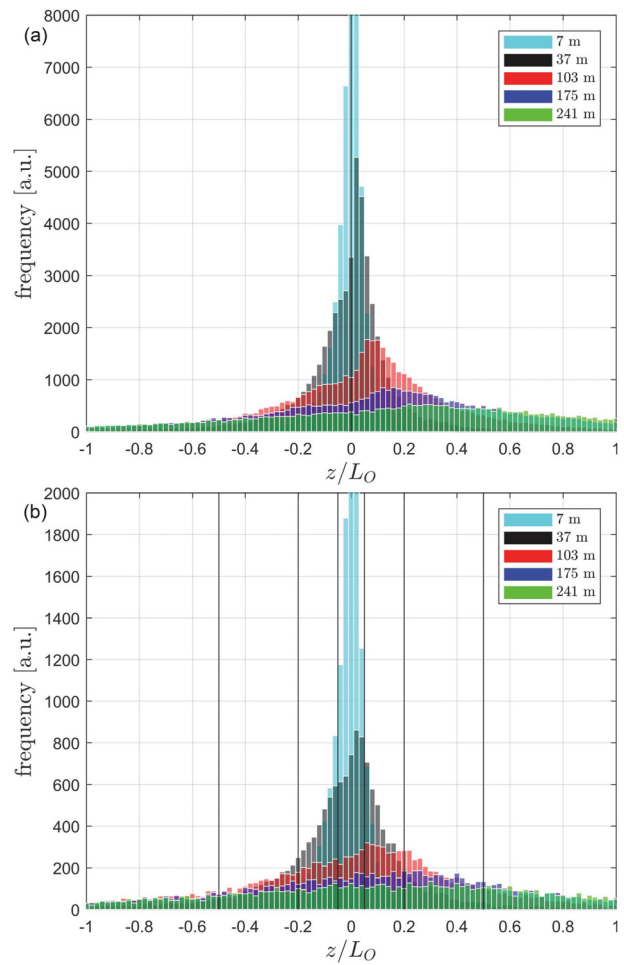


FIG. 10. Histograms of the dimensionless stability parameter for different heights for the wake- and shadow-free (a) and 270° ± 15° (b) sectors. The vertical lines show the stability ranges from Table I.

at 37 m by first fitting the vertical profile of wind speed  $U$  to the polynomial form of Höglström<sup>19</sup> from measurements of the three lowest sonic anemometers, and  $\phi_m$  is thus referred to 37 m as we use the  $u_*$  value at this level. Figure 12 shows the behavior of  $\phi_m$  with  $z/L_O$  from the sonic anemometer measurements together with the “modified” expressions of the Kansas experiment.<sup>19</sup>

As illustrated, the observed dimensionless wind shear is in good agreement with the modified Kansas expressions for all stability ranges except that the latter overpredict the dimensionless wind shear for  $z/L_O \geq 0.5$  as observed in other sites and experimental campaigns.<sup>20,21</sup> Since the behavior with the stability of the dimensionless wind shear closely follows surface-layer similarity, we can expect that by taking the ratio of the wind to the surface-layer velocity scale ( $u_*$ ), the vertical wind profile under neutral conditions follows the logarithmic wind profile within the surface layer and that both unstable and stable conditions deviate from it in accordance with surface-layer similarity. This is illustrated in Fig. 13 for all stability classes. At 7 m, the differences in the

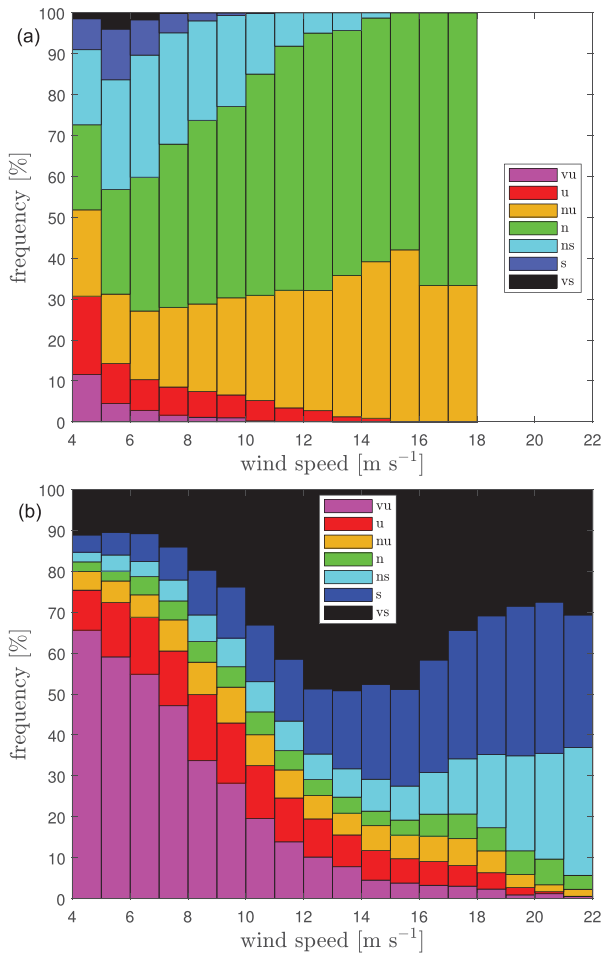


FIG. 11. Frequency of occurrence of stability classes per wind speed based on the sonic anemometer measurements at 37 m (a) and 241 m (b) for wake- and shadow-free sectors.

computed  $\langle U/u_{*37} \rangle$  values between all stability classes become small, which reflects that the roughness length is close in all stability cases; the largest discrepancies are found in very unstable and very stable conditions, as expected, since for these two ranges, atmospheric stability has a large effect on the normalized wind speed already at 7 m, and these stability ranges occur at particular months during the year, where the roughness length might be different from the all-season estimation. In the plot, the logarithmic wind profile prediction is also illustrated using the roughness length value estimated in Sec. V for the 37-m height. The prediction fits well the observations, but the latter deviates the highest we observe above the ground. This is partly because the turbulence length scale does not increase linearly with the height but has a limiting value.<sup>22</sup> It can also be seen that the standard error is the highest within the very stable case, which is due to the higher wind variability under these atmospheric conditions.

Similar to Fig. 13, we computed the turning of wind with the height for the number of stability conditions observed at the 37-m

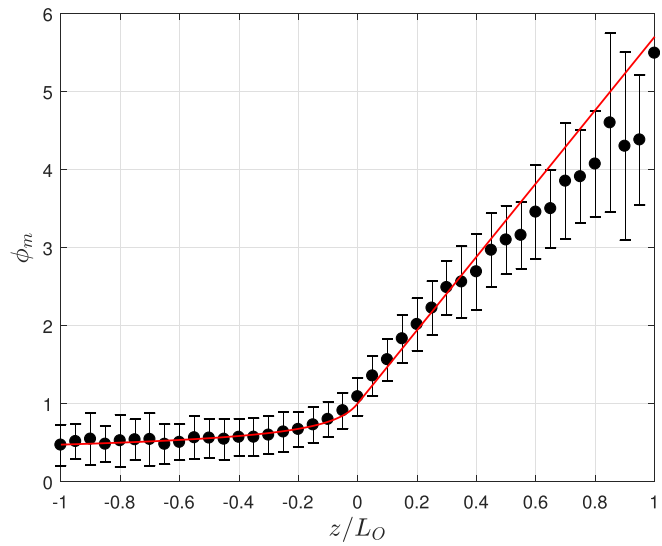


FIG. 12. Dimensionless wind shear  $\phi_m$  estimated from the lowest three sonic anemometer levels as a function of the dimensionless stability parameter  $z/L_0$  derived from the 37-m sonic anemometer within the  $270^\circ \pm 15^\circ$  sector. The solid line corresponds to the modified Kansas expressions.<sup>19</sup> The error bars correspond to  $\pm 1$  standard deviation.

level and computed the relative direction change using the 7-m level as the reference (see Fig. 14). The behavior of the turning of the wind with the height seems to be consistent with what is expected; the relative direction change mostly increases with the height (with some exceptions for the unstable classes within the two first height levels),

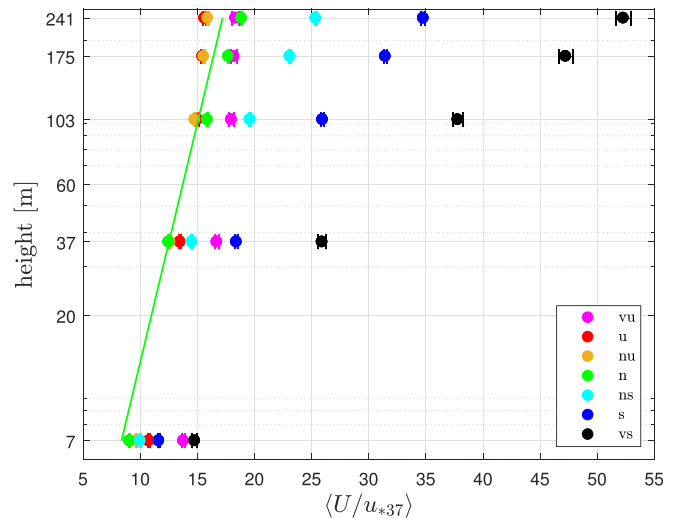


FIG. 13. Normalized mean vertical wind profiles for different atmospheric stability classes within the  $270^\circ \pm 15^\circ$  sector.  $u_{*37}$  is the friction velocity computed with the 37-m sonic anemometer. The error bars correspond to  $\pm 1$  standard error. The solid line is the prediction  $\langle U/u_{*37} \rangle = \ln(z/\exp(\ln z_0))$ , with  $z_0$  estimated from the 37-m sonic anemometer measurements for the  $270^\circ \pm 15^\circ$  sector as shown in Fig. 7(a).

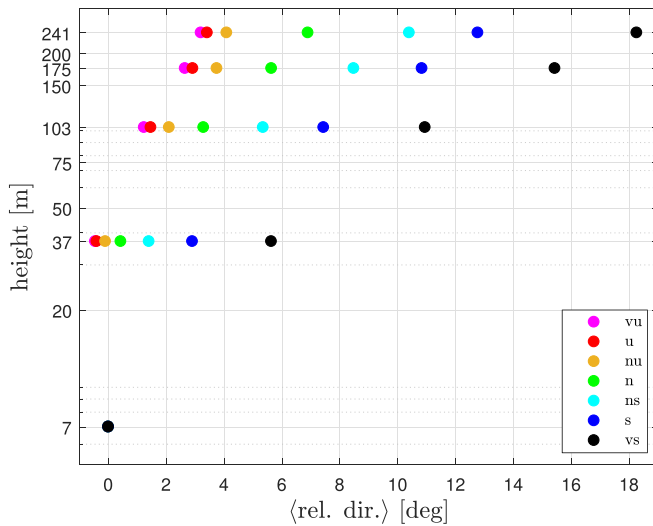


FIG. 14. Relative direction change as a function of atmospheric stability derived from the 37-m sonic anemometer within the  $270^\circ \pm 15^\circ$  sector.

with the change being the highest for very stable conditions (up to more than  $18^\circ$  at 241 m) and lowest for very unstable conditions (close to  $3^\circ$  at 241 m).

## 2. Velocity variances and covariances

Figure 15 shows the behavior with the height and stability of the three velocity variances and the  $uw$ -covariance normalized by the squared of the friction velocity at 37 m,  $u_{*37}^2$ . As expected, the highest to lowest velocity variances are those of the  $u$ -,  $v$ -, and  $w$ -velocity components, respectively, followed by the  $uw$ -covariance. The more unstable the atmosphere, the closer the  $u$ -,  $v$ -, and  $w$ -variances become; for very unstable conditions,  $\sigma_u^2 \approx \sigma_v^2 \approx \sigma_w^2$ , and for the two highest sonic levels as the atmospheric flow becomes close to isotropic. The normalized velocity variances under neutral stability conditions show the lowest values at several sonic levels.

Generally, the behavior with the height of the variances follows the same pattern; without accounting for the 7-m level, whose values can be higher or lower than those at 37 m, suggesting that local terrain features highly influence the measurements at the lowest sonic anemometer level, the velocity variances and  $uw$ -covariance decrease with the height. The only exceptions are found for very stable conditions, in which all variances and  $uw$ -covariance peak at 103 m, and for unstable and very unstable conditions for the  $w$ -variance, where there is an increasing behavior up to 175 m, as it is also normally expected for such stability conditions.<sup>23</sup> When concentrating the analysis to neutral atmospheric conditions only and to the 37-m level, the relations  $\sigma_u/u_* = 2.26$ ,  $\sigma_u/\sigma_v = 1.29$ , and  $\sigma_u/\sigma_w = 1.68$  are found, which are close to those estimated over a less rough site within an homogeneous sector.<sup>16</sup> For all close-to-neutral conditions, the ratio  $\langle u'w' \rangle / u_{*37}^2$  becomes very close to  $-1$  close to the surface, as expected from the very low contribution of the  $vw$ -covariance in  $u_*$  [see Eq. (1)].

## 3. Spectral analysis

The three velocity component autospectra and  $uw$ -cospectra were also classified into the stability classes in Table I based on  $z/L_O$  values from the 37-m sonic anemometer and then ensemble-averaged for each height. We fit the three-dimensional turbulence spectral model of Mann<sup>24</sup> (hereafter, the Mann model) to those spectra. This model is commonly used for describing atmospheric turbulence in a wide range of turbulence conditions<sup>22,25</sup> and for generating turbulence fields useful for, i.a., aeroelastic calculations.<sup>26</sup> The fitting procedure outputs the Mann model parameters, which, besides the wave vector  $\mathbf{k}$ , describe the velocity spectral tensor:  $\alpha \varepsilon^{2/3}$ ,  $L$ , and  $\Gamma$ , with  $\alpha$  being the spectral Kolmogorov constant,  $\varepsilon$  the specific rate of destruction of turbulent kinetic energy,  $L$  a length scale related to the size of the turbulent eddies, and  $\Gamma$  a parameter describing the anisotropy of the turbulence.

Figure 16 illustrates both the ensemble-averaged measured spectra and the Mann model fit for neutral conditions and for all sonic-anemometer levels. The same procedure was performed to the spectra within the other stability classes (not shown). The measured spectra behave as expected for atmospheric flow under flat and homogeneous land; the  $u$ -spectra peak the highest followed by the  $v$ - and the  $w$ -spectra, and the  $uw$ -cospectra are negative due to vertical wind shear. When moving away from the surface, the spectra peak generally lower (except for the 7-m level), indicating a decrease in the turbulence level, and the spectra peak at lower wavenumbers, indicating that the length scales are larger than those close to the surface.<sup>22</sup>

As shown, the Mann model fits well the measured spectra for all heights, with the largest differences for the  $uw$ -cospectra for which the Mann model overpredicts its energy content.<sup>27</sup> Although not shown, similar results are found under the other stability classes at all levels. Figure 17 illustrates the behavior with the height and atmospheric stability class of the Mann parameters, which were fitted from the observed spectra. In agreement with the results by Peña *et al.*<sup>22</sup> for flow over a more homogeneous and flat area, we find that  $\Gamma$  generally decreases with the height and that the relative differences with the height are larger, the more unstable the atmosphere is, reaching values about unity at the highest levels. For all stable and near-neutral stabilities, we find  $\Gamma \approx 3$ .

Also, we find that  $\alpha \varepsilon^{2/3}$  decreases with the height, as expected due to the decrease in turbulence intensity with the height being the highest the closest the atmospheric stability classes are to neutral, also as expected, as the close to neutral conditions show the highest velocity variances. Finally,  $L$ , the turbulence length scale, shows an increasing behavior with the height, as expected since the turbulent eddies also grow with the height, and the size of  $L$  is the highest the more unstable and the lowest the more stable the atmosphere is, also in very good agreement with the results obtained by Peña *et al.*<sup>22</sup> For completeness, the suggested values by IEC<sup>28</sup> for  $\Gamma$  and  $L$ , when designing wind turbines, are also shown. The measurements at Østerild show that turbulence is more isotropic and that the length scales are generally larger than the suggested values by the standard particularly the highest we observe above the ground.

An interesting question is whether or not we can estimate the Mann parameters from “traditional” measured flow parameters such as the velocity variances. Peña *et al.*<sup>22</sup> showed that the Mann-model length scale is related to the length scale of the wind profile, i.e., the

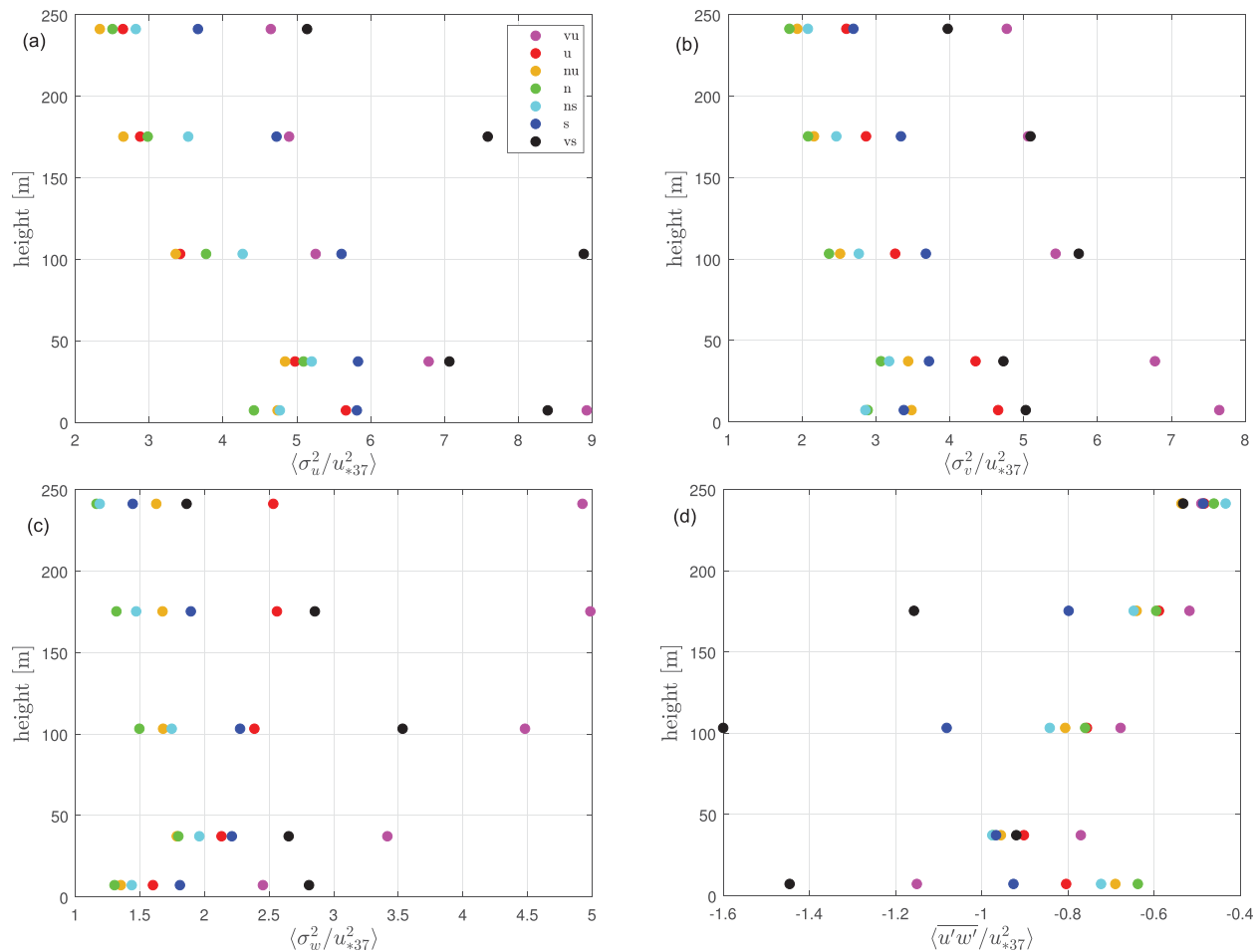


FIG. 15. Normalized variances of  $u$  (a),  $v$  (b),  $w$  (c), and  $uw$ -covariance (d) as a function of height and atmospheric stability derived from the 37-m sonic anemometer within the  $270^\circ \pm 15^\circ$  sector.

mixing-length scale, which from mixing-length theory is the ratio of the friction velocity to the vertical wind shear. They showed that for a range of atmospheric stability conditions, wind speed ranges, and heights,  $L \approx 1.70u_* / (dU/dz)$ . Kelly<sup>9</sup> proposed the relation  $L \approx \sigma_u / (dU/dz)$ , which can be computed directly from cup anemometer measurements. Figure 18 shows the behavior of  $L$  with the latter relation for a number of atmospheric stability conditions and heights.  $L$  behaves linearly with both ratios within all stable and close to neutral ranges. Under unstable and very unstable regimes at the two highest measurement levels, the behavior is not linear mainly due to the very low vertical wind shear.

### VII. CONCLUSIONS AND PERSPECTIVES

The Østerild test station provides us with a high-quality, long-term, and accurate dataset of meteorological measurements. Such measurements are needed for the evaluation and improvement of meteorological and turbulence models. We showed that, in particular, the dataset from the southernmost lighting mast allows us to study the long-term wind climatology and its

variation, which is required, e.g., in wind resource assessment. It was shown that the winds at Østerild experience all types of atmospheric stability conditions during the year, which is useful to understand the behavior of the mean wind and direction and turbulence within a wide range of flow conditions. Particularly, for the predominant winds, we argued that the flow can be considered homogeneous and showed that close to the surface, it follows Monin-Obukhov similarity. The velocity variances and  $uw$ -covariance showed the expected behavior with both stability and height. Finally, spectral analysis revealed the behavior of the velocity spectral tensor characteristics with both the height and stability, and it was further demonstrated that the turbulence length scale is linearly related to the variance of the wind and the vertical wind shear.

Evaluation of meteorological models, ranging from meso- to microscales, and microscale flow models of different fidelities, ranging from linearized Navier-Stokes equations to large-eddy simulations, is currently undergoing using the Østerild measurements. The particular predominant westerlies at the south lightning mast allow us the

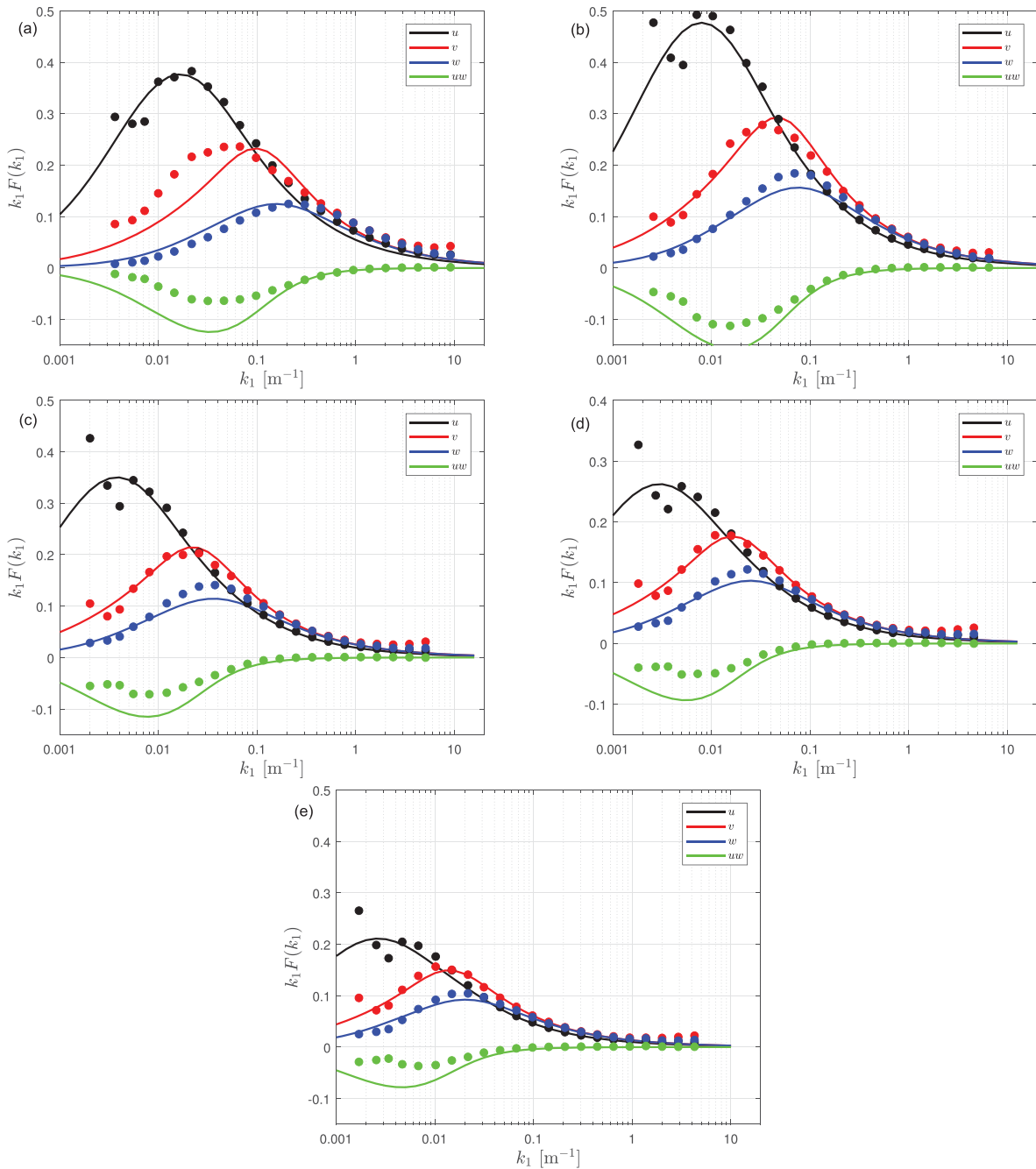


**FIG. 16.** Power spectrum of the three velocity components and the  $uw$ -cospectrum, as function of wavenumber within the  $270^\circ$  sector and for neutral stability conditions as measured by the 37-m sonic anemometer. The markers show the ensemble-average measured spectra and the solid lines the fit using the Mann model. Each frame shows a different sonic anemometer level: (a) 7, (b) 37, (c) 103, (d) 175, and (e) 241 m.

comparison of idealized simulations of canonical flows and help understanding the behavior of the models over close to homogeneous conditions. The heterogeneity of the area challenges the microscale model abilities. Also of particular interest is to evaluate the accuracy of meso-micro-coupling techniques at Østerild. Inputs to mesoscale

models, such as land use information, face challenges for representing the heterogeneity of the area and show the need to properly downscale from the meso- to the microscales. Work in progress is related to determining what kind of inputs (e.g., land use, boundary, and initial conditions) both types of models should use to get the most accurate

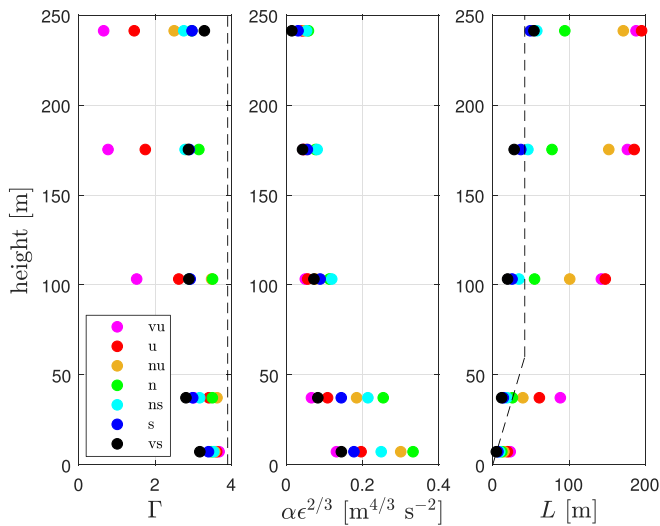


FIG. 17. The behavior of the Mann parameters as a function of height and atmospheric stability conditions as measured by the 37-m sonic anemometer. The dashed lines show the suggestions by IEC.<sup>28</sup>

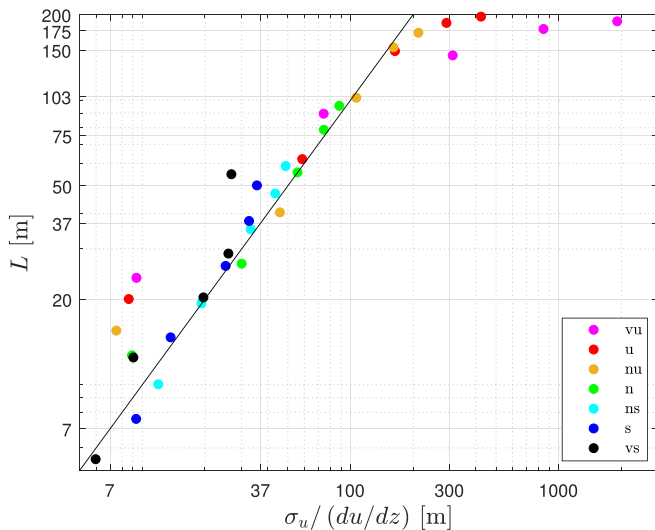


FIG. 18. The length scale of the Mann model  $L$  and its relationship with the ratio of the  $u$ -velocity standard deviation to the vertical wind shear for a number of atmospheric stability classes, as measured by the 37-m sonic anemometer, and heights (markers). The solid line shows the 1:1 relation suggested by Kelly.<sup>9</sup>

coupling result. Remote-sensing techniques, i.e., wind and aerial lidars, and satellite information, are constantly being used at Østerild to characterize both the flow beyond the range of the mast and the surface heterogeneity.

### ACKNOWLEDGMENTS

This work was partly funded by the Ministry of Foreign Affairs of Denmark and administered by the Danida Fellowship Centre

through the “Multiscale and Model-Chain Evaluation of Wind Atlases” (MEWA) project. This work was also partly funded by the “Virtual Atmosphere” cross-cutting activity at DTU Wind Energy. The roughness length map around the Østerild area is a contribution from Ebba Dellwik, who is here acknowledged. Andrea N. Hahmann is also acknowledged for her comments on this manuscript.

### REFERENCES

- <sup>1</sup>T. W. Horst, S. R. Semmer, and G. Maclean, “Correction of a non-orthogonal, three-component sonic anemometer for flow distortion by transducer shadowing,” *Boundary-Layer Meteorol.* **155**, 371–395 (2015).
- <sup>2</sup>A. Peña, E. Dellwik, and J. Mann, “A method to assess the accuracy of sonic anemometer measurements,” *Atmos. Meas. Tech.* **12**, 237–252 (2019).
- <sup>3</sup>K. McCaffrey, P. T. Quelet, A. Choukulkar, J. M. Wilczak, D. E. Wolfe, S. P. Oncley, W. A. Brewer, M. Debnath, R. Ashton, G. V. Iungo, and J. K. Lundquist, “Identification of tower-wake distortions using sonic anemometer and lidar measurements,” *Atmos. Meas. Tech.* **10**, 393–407 (2017).
- <sup>4</sup>J. Mann, J.-P. Cariou, M. S. Courtney, R. Parmentier, T. Mikkelsen, R. Wagner, P. Lindelöw, M. Sjöholm, and K. Enevoldsen, “Comparison of 3D turbulence measurements using three staring wind lidars and a sonic anemometer,” *Meteorol. Z.* **18**, 135–140 (2009).
- <sup>5</sup>A. Peña, J. Mann, and N. Dimitrov, “Turbulence characterization from a forward-looking nacelle lidar,” *Wind Energy Sci.* **2**, 133–152 (2017).
- <sup>6</sup>X. G. Larsén, E. L. Petersen, and S. E. Larsen, “Variation of boundary-layer wind spectra with height,” *Q. J. R. Meteorol. Soc.* **144**, 2054–2066 (2018).
- <sup>7</sup>I. Karagali, J. Mann, E. Dellwik, and N. Vasiljevic, “New European wind atlas: The Østerild balconies experiment,” *J. Phys.: Conf. Ser.* **1037**, 052029 (2018).
- <sup>8</sup>J. Mann, N. Angelou, J. Arnqvist, D. Callies, E. Cantero, R. C. Arroyo, M. Courtney, J. Cuxart, E. Dellwik, J. Gottschall, S. Ivanell, P. Kühn, G. Lea, J. Matos, J. Palma, L. Pauscher, A. Peña, J. S. Rogrigo, S. Södeberg, N. Vasiljevic, and C. V. Rogdriguez, “Complex terrain experiments in the New European Wind Atlas,” *Philos. Trans. R. Soc. A* **375**, 20160101 (2017).
- <sup>9</sup>M. Kelly, “From standard measurements to spectral characterization: Turbulence length scale and distribution,” *Wind Energy Sci.* **3**, 533–543 (2018).
- <sup>10</sup>A. Hannesdóttir and M. Kelly, “Detection and characterization of extreme wind speed ramps,” *Wind Energy Sci.* **4**, 385–396 (2019).
- <sup>11</sup>METEK GmbH, *Flow Distortion Correction for 3-D Flows as Measured by METEK’s Ultrasonic Anemometer USA-1* (METEK GmbH, 2004).
- <sup>12</sup>H. Liu, G. Peters, and T. Foken, “New equations for sonic temperature variance and buoyancy heat flux with an omnidirectional sonic anemometer,” *Boundary-Layer Meteorol.* **100**, 459–468 (2001).
- <sup>13</sup>S.-E. Gryning, R. Floors, A. Peña, E. Batchvarova, and B. Brümmner, “Weibull wind-speed distribution parameters derived from a combination of wind-lidar and tall-mast measurements over land, coastal and marine areas,” *Boundary-Layer Meteorol.* **159**, 329–348 (2016).
- <sup>14</sup>R. Floors, P. Enevoldsen, N. Davis, J. Arnqvist, and E. Dellwik, “From lidar scans to roughness maps for wind resource modelling in forested areas,” *Wind Energy Sci.* **3**, 353–370 (2018).
- <sup>15</sup>J. R. Garratt, *The Atmospheric Boundary Layer* (Cambridge University Press, New York, USA, 1992).
- <sup>16</sup>A. Peña, P.-E. Réthoré, and M. P. V. der Laan, “On the application of the Jensen wake model using a turbulence-dependent wake decay coefficient: The Sexbierum case,” *Wind Energy* **19**, 763–776 (2016).
- <sup>17</sup>A. S. Monin and A. M. Obukhov, “Osnovnye zakonomernosti turbulentnogo peremeshivaniya v prizemnom sloe atmosfery (Basic laws of turbulent mixing in the atmosphere near the ground),” *Tr. Geofiz. Inst., Akad. Nauk SSSR* **24**, 163–187 (1954).
- <sup>18</sup>A. J. Dyer, “A review of flux-profile relationships,” *Boundary-Layer Meteorol.* **7**, 363–372 (1974).
- <sup>19</sup>U. Högström, “Non-dimensional wind and temperature profiles in the atmospheric surface layer: A re-evaluation,” *Boundary-Layer Meteorol.* **42**, 55–78 (1988).

- <sup>20</sup>Y. Cheng and W. Brutsaert, "Flux-profile relationships for wind speed and temperature in the stable atmospheric boundary layer," *Boundary-Layer Meteorol.* **114**, 519–538 (2005).
- <sup>21</sup>A. Peña, R. Floors, A. Sathe, S.-E. Gryning, R. Wagner, M. S. Courtney, X. G. Larsén, A. N. Hahmann, and C. B. Hasager, "Ten years of boundary-layer and wind-power meteorology at Høvsøre, Denmark," *Boundary-Layer Meteorol.* **158**, 1–26 (2016).
- <sup>22</sup>A. Peña, S.-E. Gryning, and J. Mann, "On the length-scale of the wind profile," *Q. J. R. Meteorol. Soc.* **136**, 2119–2131 (2010).
- <sup>23</sup>R. B. Stull, *An Introduction to Boundary Layer Meteorology* (Kluwer Academic Publishers, 1988), p. 666.
- <sup>24</sup>J. Mann, "The spatial structure of neutral atmospheric surface-layer turbulence," *J. Fluid Mech.* **273**, 141–168 (1994).
- <sup>25</sup>A. Chougule, J. Mann, A. Segalini, and E. Dellwik, "Spectral tensor parameters for wind turbine load modeling from forested and agricultural landscapes," *Wind Energy* **18**, 469–481 (2015).
- <sup>26</sup>N. Dimitrov, M. C. Kelly, A. Vignaroli, and J. Berg, "From wind to loads: Wind turbine site-specific load estimation with surrogate models trained on high-fidelity load databases," *Wind Energy Sci.* **3**, 767–790 (2018).
- <sup>27</sup>A. Peña, S.-E. Gryning, J. Mann, and C. B. Hasager, "Length scales of the neutral wind profile over homogeneous terrain," *J. Appl. Meteorol. Climatol.* **49**, 792–806 (2010).
- <sup>28</sup>IEC, *IEC 61400-1: Wind Turbines-Part 1: Design Requirements* (International Standard, International Electrotechnical Commission, Geneva, Switzerland, 2005).